Helicity cascades in rotating turbulence

P. D. Mininni[1,2] and A. Pouquet[2]
[1]*Departamento de Física, Facultad de Ciencias Exactas y Naturales, Universidad de Buenos Aires, Ciudad Universitaria, 1428 Buenos Aires, Argentina*
[2]*NCAR, P.O. Box 3000, Boulder, Colorado 80307-3000, USA*
(Received 4 September 2008; published 5 February 2009)

The effect of helicity (velocity-vorticity correlations) is studied in direct numerical simulations of rotating turbulence down to Rossby numbers of 0.02. The results suggest that the presence of net helicity plays an important role in the dynamics of the flow. In particular, at small Rossby number, the energy cascades to large scales, as expected, but helicity then can dominate the cascade to small scales. A phenomenological interpretation in terms of a direct cascade of helicity slowed down by wave-eddy interactions leads to the prediction of non-Kolmogorovian inertial indices for the small-scale energy and helicity spectra.

DOI: 10.1103/PhysRevE.79.026304 PACS number(s): 47.32.Ef, 47.27.Gs, 47.27.Jv

I. INTRODUCTION

Invariants of the equations of motion play an essential role in the behavior of turbulent flows. The well-known cascade of energy to the small scales in three-dimensional hydrodynamic turbulence, associated with the energy invariant, has been studied at length since the celebrated paper of Kolmogorov [1]. Less well understood is the role played by the second quadratic (but nonpositive definite) invariant of the Euler equations, namely, the helicity which embodies the global correlations between the velocity field $\mathbf{u}$ and the vorticity $\boldsymbol{\omega}=\nabla\times\mathbf{u}$. Helicity itself plays no role in the Kolmogorov (K41) theory of turbulence [1]. Shortly after the discovery that helicity is a quadratic invariant of the three-dimensional Euler equation [2] (see also Ref. [3]), two scenarios were put forward for its dynamical behavior [4]: a dual cascade of energy and helicity towards smaller scales and a pure helicity cascade with no cascade of energy. Studies of absolute equilibrium ensembles for isotropic helical turbulence [5] gave support to the former scenario, a result that was later confirmed by two-point closure models of turbulence [6] as well as by direct numerical simulations (DNS) [7–11].

In nonrotating helical hydrodynamic turbulence, both the helicity and the energy cascade towards smaller scales with constant fluxes. The assumption that the transfer rates are determined by the energy flux alone gives Kolmogorov scaling in the inertial range of both quantities, as is observed in the numerical simulations. As a result, the presence of helicity may globally arrest the energy transfer (when $\mathbf{u}$ is strictly parallel to $\boldsymbol{\omega}$, the nonlinear term—expressed in terms of the Lamb vector $\mathbf{u}\times\boldsymbol{\omega}$—is zero to within a pressure term), but the energy cascade scaling does not differ from that of nonhelical turbulence.

In rotating turbulence, helicity is still an inviscid quadratic invariant. Perhaps because of the existence of dual direct cascades in nonrotating turbulence, not much attention has been paid in the literature to the scaling of net helicity in the rotating case. Helical-wave decompositions were introduced in Refs. [12,13] (see also Refs. [14,15]) and were found useful in the study of rotating turbulence [16,17]. Theoretical predictions for the helicity spectrum in the presence of strong rotation were also given in Ref. [18] in the framework of weak turbulence, under the assumption of a dual cascade. Recently, the effect of helicity in free-decaying rotating turbulence was studied in numerical simulations [19]. It was observed that both effects inhibit the energy transfer through different mechanisms: helicity diminishes nonlinear interactions globally, whereas rotation concentrates nonlinear interactions to resonant triads of inertial waves.

The lack of detailed studies of rotating helical flows is remarkable considering the relevance of helicity in certain atmospheric processes [20–22], such as rotating convective (supercell) thunderstorms the predictability of which may be enhanced because of the increased stability associated to the weakening of the nonlinear terms. Recently, high-resolution numerical simulations of rotating flows with nonhelical forcing [23] showed that, while the velocity and vorticity in real space develop anisotropies and large-scale columnlike structures as expected, the spatial distribution of helicity is more homogeneous and isotropic and tends to have a short correlation length. This observation motivates the present study. We present results from DNS of rotating turbulent flows with helical forcing and moderate rotation. The results suggest that rotating helical flows behave in a different way than rotating nonhelical flows. In particular, an inverse cascade of energy and a direct cascade of energy and helicity are discussed, the latter, novel insofar as the transfer rate to small scales, is dominated by the helicity flux.

II. NUMERICAL SIMULATIONS

We solve numerically the equations for an incompressible rotating fluid with constant mass density

$$\frac{\partial\mathbf{u}}{\partial t}+\boldsymbol{\omega}\times\mathbf{u}+2\boldsymbol{\Omega}\times\mathbf{u}=-\nabla\mathcal{P}+\nu\nabla^2\mathbf{u}+\mathbf{F} \tag{1}$$

and

$$\nabla\cdot\mathbf{u}=0, \tag{2}$$

where $\mathbf{u}$ is the velocity field, $\boldsymbol{\omega}=\nabla\times\mathbf{u}$ is the vorticity, $\mathcal{P}$ is the total pressure (modified by the centrifugal term) divided by the mass density, and ν is the kinematic viscosity. Here, $\mathbf{F}$

TABLE I. Parameters used in the simulations. k_F gives the range of forcing wave numbers, ν is the kinematic viscosity, and Ω the rotation rate; Re, Ro, and Ek are, respectively, the Reynolds, Rossby, and Ekman numbers. Runs are performed on grids of 512^3 points in all cases and up to 40 turn-over times.

Run	k_F	ν	Ω	Re	Ro	Ek
A1	7-8	6.5×10^{-4}	0.06	1200	7.9	6.5×10^{-3}
A2	7-8	6.5×10^{-4}	0.3	1200	1.6	1×10^{-3}
A3	7-8	6.5×10^{-4}	7	1200	0.07	6×10^{-5}
A4	7-8	6.5×10^{-4}	14	1200	0.03	2.5×10^{-5}
B1	2-3	6×10^{-4}	0.08	5700	2.1	4×10^{-4}
B2	2-3	6×10^{-4}	3.5	5700	0.05	9×10^{-6}
B3	2-3	6×10^{-4}	8	5700	0.02	3.5×10^{-6}

is an external force that drives the turbulence, and we choose the rotation axis to be in the z direction: $\mathbf{\Omega}=\Omega\hat{z}$, with Ω the rotation frequency.

Equation (1) is solved using a parallel pseudospectral code in a three dimensional box of size 2π with periodic boundary conditions and with a spatial resolution of 512^3 regularly spaced grid points. The pressure is obtained by taking the divergence of Eq. (1), using the incompressibility condition (2), and solving the resulting Poisson equation. The equations are evolved in time using a second order Runge-Kutta method, and the code uses the 2/3 rule for dealiasing. As a result, the maximum wave number is $k_{\max}=N/3$ where N is the number of grid points in each direction. The code is fully parallelized with the message passing interface (MPI) library [24,25].

The mechanical forcing $\mathbf{F}$ in Eq. (1) is given by the Arn'old-Beltrami-Childress (ABC) flow [26]

$$\mathbf{F}=F_0\{[B\cos(k_F y)+C\sin(k_F z)]\hat{x}+[C\cos(k_F z)+A\sin(k_F x)]\hat{y}+[A\cos(k_F x)+B\sin(k_F y)]\hat{z}\}, \quad (3)$$

where F_0 is the forcing amplitude, $A=0.9$, $B=1$, $C=1.1$ [27], and k_F is the forcing wave number. The ABC flow is an eigenfunction of the curl with eigenvalue k_F; as a result, when used as a forcing function, it injects both energy and helicity in the flow. It should be noted that in homogeneous turbulence the helicity spectrum cannot develop if it is initially zero (see, e.g., Refs. [12,16]), or if an external mechanism does not inject helicity. In nature, helicity is created, e.g., in the presence of rotation and stratification [28], or near solid boundaries in rotating vessels [29]. The use of the ABC forcing, although artificial, allows us to study helical rotating turbulence without the extra computational cost associated to the presence of boundaries or stratification.

The Reynolds, Rossby, and Ekman numbers are defined as usual as

$$\mathrm{Re}=\frac{L_F U}{\nu}, \quad (4)$$

$$\mathrm{Ro}=\frac{U}{2\Omega L_F}, \quad (5)$$

and

$$\mathrm{Ek}=\frac{\mathrm{Ro}}{\mathrm{Re}}=\frac{\nu}{2\Omega L_F^2}. \quad (6)$$

where $L_F=2\pi/k_F$, and the turnover time at the forcing scale is then defined as $T=L_F/U$ where $U=\langle u^2\rangle$ is the r.m.s. velocity measured in the turbulent steady state or when the inverse cascade of energy starts (see below). The dissipation wave numbers k_η quoted below correspond to the Kolmogorov wave number $k_\eta=(\epsilon/\nu^3)^{1/4}$, where ϵ is the energy injection rate.

In the following, it will be useful to introduce a micro-Rossby number as the ratio of the r.m.s. vorticity to the background vorticity (rotation)

$$\mathrm{Ro}_\omega=\frac{\omega}{2\Omega}. \quad (7)$$

The value of the micro-Rossby number plays a central role in the inhibition of the energy cascade in rotating turbulence [16]. If the micro-Rossby number is too small, nonlinear interactions are completely damped. According to Ref. [30], anisotropies develop in rotating flows when the Rossby number $\mathrm{Ro}\lesssim 1$ and when the micro-Rossby number $\mathrm{Ro}_\omega\gtrsim 1$ (it is worth noting that the actual values for the transition depend on the particular flow studied). We are therefore interested in flows with large Reynolds numbers, but with moderate Rossby numbers as often encountered in geophysical problems. As an example, the Rossby number for midlatitude synoptic scales in the atmosphere is $\mathrm{Ro}\approx 0.1$. Realistic values of the Reynolds numbers in DNS are of course unattainable with present day computers, while the limit of very small Rossby number is better studied with wave-turbulence theory (see, e.g., Ref. [18]).

Table I gives the parameters used in the simulations. All runs are well resolved and were continued for over 40 turnover times. Runs A1 and B1 were started from a fluid at rest, while the rest of the runs in sets A and B were started from the turbulent steady state reached at the end of runs A1 and B1, respectively.

Given the velocity field from any of these runs, we define the isotropic energy spectrum as

$$E(k) = \frac{1}{2} \sum_{k \leqslant |\mathbf{k}| < k+1} \hat{\mathbf{u}}^*(\mathbf{k}) \cdot \hat{\mathbf{u}}(\mathbf{k}), \tag{8}$$

where $\hat{\mathbf{u}}(\mathbf{k})$ is the Fourier transform of the velocity field, $\mathbf{k}$ is the wave vector, and the asterisk denotes complex conjugate. The isotropic helicity spectrum can also be defined as

$$H(k) = \frac{1}{2} \sum_{k \leqslant |\mathbf{k}| < k+1} \hat{\mathbf{u}}^*(\mathbf{k}) \cdot \hat{\boldsymbol{\omega}}(\mathbf{k}), \tag{9}$$

where $\hat{\boldsymbol{\omega}}(\mathbf{k})$ is the Fourier transform of the vorticity field, and it is assumed that the complex conjugate of the term on the right-hand side (RHS) is added to obtain a real spectrum. Note the sums in these expressions run over spherical shells in Fourier space. Reduced energy and helicity spectra as a function of wave numbers $k_\perp$ with $\mathbf{k}_\perp = (k_x, k_y, 0)$, and $k_\parallel$ with $\mathbf{k}_\perp = (0, 0, k_z)$, can be defined by computing the sums respectively over cylinders and over planes (see Ref. [23] for more details).

The energy integral scale is then given by

$$L = 2\pi \frac{\sum_{k=1}^{k_{\max}} E(k) k^{-1}}{\sum_{k=1}^{k_{\max}} E(k)}. \tag{10}$$

An integral scale for the helicity can also be defined as

$$L^H = 2\pi \frac{\sum_{k=1}^{k_{\max}} H(k) k^{-1}}{\sum_{k=1}^{k_{\max}} H(k)}. \tag{11}$$

Perpendicular and parallel integral scales (e.g., $L_\perp$ and $L_\parallel$) are useful to measure the development of anisotropies and are defined by replacing k by $k_\perp$ or $k_\parallel$ in Eqs. (10) and (11).

To determine the direction of the cascades in the simulations, it is useful to study the energy and helicity fluxes. For the isotropic case, these are, respectively, defined as

$$\Pi(K) = \sum_{k=1}^{K} T(k), \tag{12}$$

$$\Sigma(K) = \sum_{k=1}^{K} T^H(k), \tag{13}$$

where $T(k)$ and $T^H(k)$ are the transfer functions for the energy and the helicity

$$T(k) = \sum_{k \leqslant |\mathbf{k}| < k+1} \hat{\mathbf{u}}^*(\mathbf{k}) \cdot \widehat{(\mathbf{u} \times \boldsymbol{\omega})}, \tag{14}$$

$$T^H(k) = \sum_{k \leqslant |\mathbf{k}| < k+1} \hat{\boldsymbol{\omega}}^*(\mathbf{k}) \cdot \widehat{(\mathbf{u} \times \boldsymbol{\omega})}. \tag{15}$$

Here, as in the case of the helicity spectrum, it is assumed the complex conjugate of the terms on the RHS is added to obtain real transfer functions. Reduced transfer functions and fluxes in terms of $k_\perp$ and $k_\parallel$ can also be studied with the procedure described above.

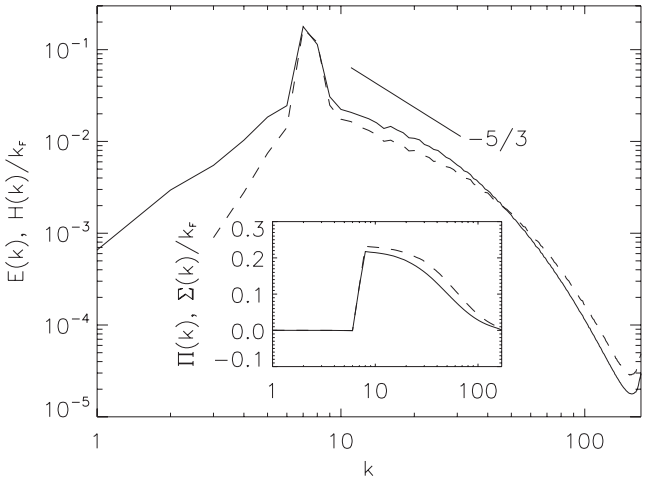

FIG. 1. Energy (solid line) and helicity (dash line) spectra in run A2 with forcing around $k \approx 7.5$ and almost negligible rotation. The inset shows the energy and helicity fluxes indicative of two classical direct cascades.

III. NUMERICAL RESULTS

A. Energy inverse cascade at low Rossby numbers

For strong rotation, it is known that the flow becomes quasi-two-dimensional and an inverse cascade of energy is expected [12,13]. Figure 1 shows the energy and helicity spectra at late times in run A2, for a moderate Rossby number, as well as their fluxes. One observes that the flux of energy $\Pi(k)$ and of helicity $\Sigma(k)$ are both negligible for $k < k_F$ and are of order unity and positive at wave numbers larger than the forcing wave number k_F (here and in the following, the helicity spectrum and flux are plotted normalized by the forcing wave number k_F, to have them of the same order than the energy spectrum and flux when helicity injection is maximal). The inertial ranges of both the energy and helicity show similar scaling, close to K41 except for bottleneck (and possibly intermittency) corrections. Similar results are obtained in run A1 which has hardly any rotation effect.

However, runs A3 and A4 at low Rossby number show a different behavior (see Fig. 2): at scales larger than the forcing scale, an inverse cascade of energy is observed, with constant and negative energy flux, and with its amplitude roughly an order of magnitude larger than in the large Rossby number case. However, the spectrum of helicity in this inverse range is approximately flat, and the flux of helicity towards large scales is almost negligible.

The development of anisotropies and the inverse cascade of energy in rotating flows, leading, for example, to zonal flows in planetary atmospheres, has been explained in terms of near-resonant triad interactions of inertial waves: energy in three dimensional modes is transferred by a subset of the resonant interactions to modes with smaller vertical wave number [12,13], a process that drives the flow to be quasi-

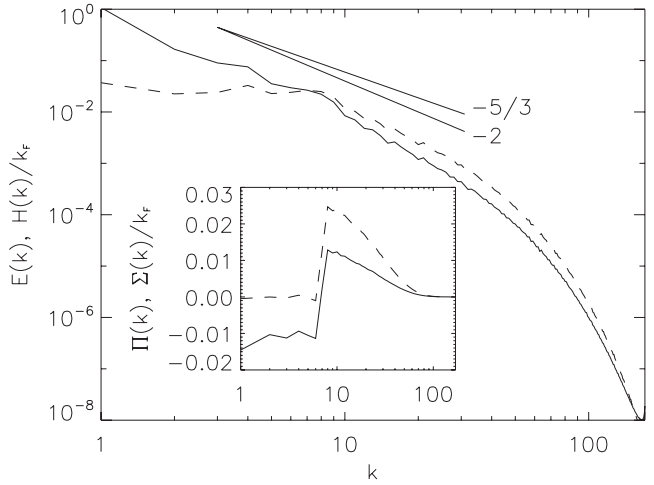

FIG. 2. Energy (solid) and helicity (dash) spectra in run A3 with the same forcing as run A2 but lower Rossby number. Different slopes are shown as a reference. The inset gives the energy and helicity fluxes and shows that there is both a direct and an inverse cascade of energy but only a direct cascade of helicity.

two-dimensional at large scales. The lack of an inverse transfer of helicity to large scales can be understood considering the partial two dimensionalization of the flow at large scales: a helical flow is three dimensional, while a two-dimensional flow has no helicity. Indeed, the energy spectra and fluxes in the direction perpendicular to $\mathbf{\Omega}$ are similar to the isotropic spectrum (see Fig. 3), while the spectrum in the direction parallel to $\mathbf{\Omega}$ peaks at $k_\parallel=0$ (details of how much energy is in the modes with $k_\parallel=0$ in each run are given in Table II).

The absence of an inverse cascade of helicity is further confirmed by the time evolution of the total energy, helicity and enstrophy (see Fig. 4). While the energy increases monotonically after $t\approx 10$, the helicity and the enstrophy decay until reaching a steady state after $t\approx 25$. The monotonic increase of the total energy is the result of the piling up of energy at $k_\perp=1$ as the inverse cascade develops over time.

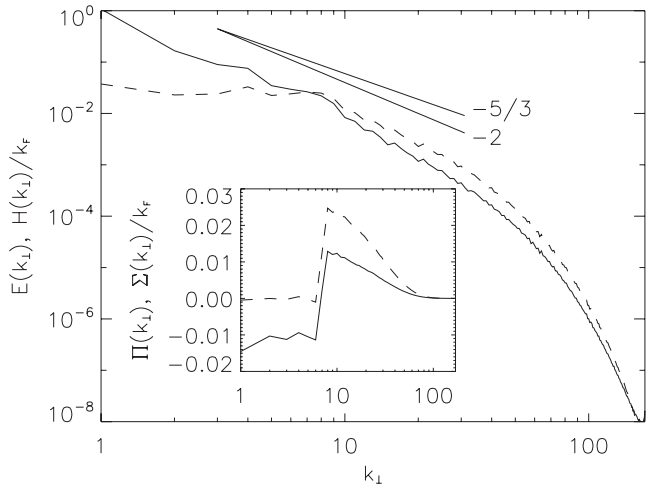

FIG. 3. Energy (solid) and helicity (dash) spectra as a function of $k_\perp$ in run A3. Different slopes are shown as a reference. The inset shows the energy and helicity fluxes in terms of $k_\perp$.

TABLE II. Anisotropies measured at $t\approx 40$ in all runs. Ro_ω is the micro-Rossby number as defined in Eq. (7), $L_\perp/L_\parallel$ is the ratio of perpendicular to parallel integral scales as defined in Eq. (10), $L_\perp^H/L_\parallel^H$ is the same ratio but based on the helicity spectrum as in Eq. (11), $E(k_\parallel=0)/E$ is the ratio of energy in all modes with $k_\parallel=0$ to the total energy, and $H(k_\parallel=0)/H$ is the ratio of helicity in those modes to the total helicity.

Run	Ro_ω	$L_\perp/L_\parallel$	$L_\perp^H/L_\parallel^H$	$E(k_\parallel=0)/E$	$H(k_\parallel=0)/H$
A1	160	0.56	0.56	0.05	0.04
A2	31	0.55	0.55	0.06	0.05
A3	0.6	1.28	0.53	0.95	0.74
A4	0.2	1.27	0.49	0.98	0.90
B1	95	0.86	0.85	0.30	0.33
B2	1.1	1.51	1.20	0.96	0.85
B3	0.5	1.36	1.07	0.96	0.86

However, the distributions of both the energy and the helicity become anisotropic as time evolves. Table II gives the micro-Rossby number for all the runs at $t\approx 40$, the ratios of perpendicular to parallel integral scales for the energy and for the helicity $L_\perp/L_\parallel$ and $L_\perp^H/L_\parallel^H$, and finally the amount of energy and helicity in the modes with $k_\parallel=0$ normalized, respectively, by the total energy and helicity. As the Rossby number decreases, the ratios $L_\perp/L_\parallel$ and $L_\perp^H/L_\parallel^H$ increase. However, the ratio of scales based on the helicity is smaller than the ratio of scales based on the energy, specially in the runs in set A where there is a larger separation between the largest scale in the box and the injection scale. This trend is accompanied by an increase in the amount of energy and helicity in the modes with $k_\parallel=0$, although here again the ratio $E(k_\parallel=0)/E$ is larger than $H(k_\parallel=0)/H$. This can be understood in terms of the Schwarz inequality for each mode in Fourier space. As the energy undergoes an inverse cascade, some helicity is transferred to the large scales (note the flat spectrum of helicity at large scales in Fig. 2 compared with the

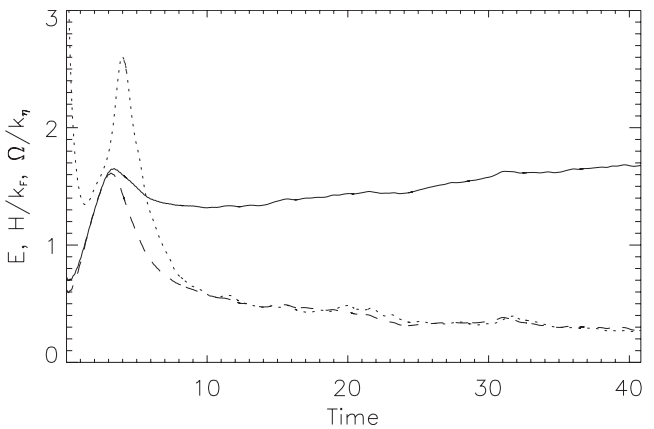

FIG. 4. Time evolution of the energy (solid), helicity (dash), and enstrophy (dot) in run A3. The helicity is normalized by k_F, and the enstrophy is rescaled by the dissipation wave number $k_\eta\approx 100$. Only the energy undergoes an inverse cascade, thereby growing with time.

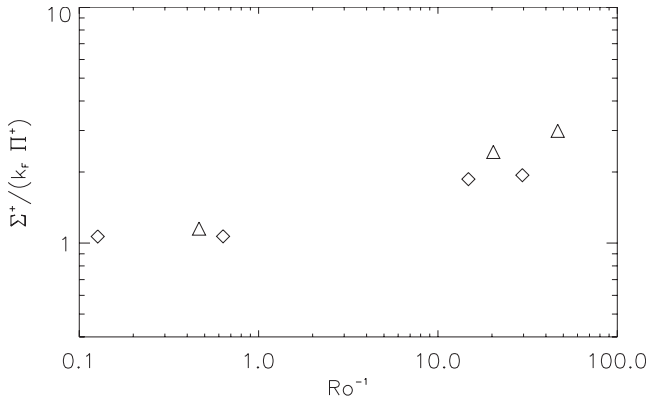

FIG. 5. Ratio of helicity flux to energy flux towards small scales as a function of inverse Rossby number and at a fixed Reynolds number for each set (see Table I). Diamonds correspond to runs in set A, and triangles correspond to runs in set B. Note the increase in relative strength of the helicity cascade to small scales as rotation increases.

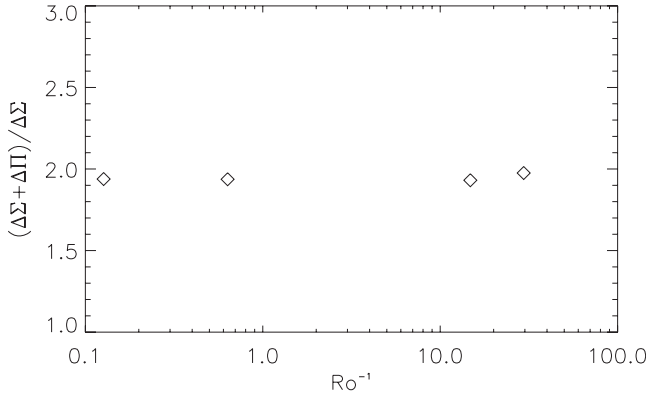

FIG. 6. Sum for the energy and helicity of the normalized differences between their direct and inverse fluxes (see text). Only runs in set A (diamonds) are shown because runs in set B do not have enough scale separation between the forcing and the largest scale in the box to compute Σ^- and Π^- reliably.

steep spectrum in Fig. 1). According to the instability assumption of Ref. [13] (see also Refs. [31,12]), the energy is transferred toward modes with wave vectors perpendicular to the rotation axis. From the Schwarz inequality, the helicity in each wave mode $\mathbf{k}$ must satisfy $|H(\mathbf{k})| \leqslant |\mathbf{k}|E(\mathbf{k})$, and the large scale helicity must be transferred towards $k_\perp$ to satisfy this relation.

B. The case for direct cascades

At scales smaller than the forcing scale, the energy spectrum in runs A3 and A4 at low Rossby numbers is slightly steeper than k^{-2} (see Fig. 3) and (unlike the case of nonrotating turbulence), the helicity spectrum is possibly shallower than the energy spectrum (a confirmation of this using runs in set B is discussed below). Furthermore (see Fig. 5), the energy flux $\Pi(k)$ becomes smaller than the (normalized) helicity flux $\Sigma(k)/k_F$ at wave numbers larger than k_F as the Rossby number is decreased.

This change can be understood as follows. The energy injection rate ϵ and the helicity injection rate δ are related by $\delta \sim k_F \epsilon$ (these two quantities are equal when maximally helical forcing is applied at a single wave number). The Schwarz inequality in each shell $|H(k)| \leqslant kE(k)$ implies that, at large scale (in the limit $k \to 0$), there must be a negligible flux of helicity [unless, of course, $E(k) \to \infty$]; thus helicity is bound to cascade to small scales. However, the development of an inverse cascade of energy decreases the amount of energy flux that can go to small scales, and as a result the helicity flux dominates for $k > k_F$. This can be illustrated by plotting the ratio $\Sigma^+/(k_F \Pi^+)$ (Fig. 5), where Σ^+ and Π^+ denote, respectively, the amount of helicity and energy flux that goes towards small scales. Note that $\Sigma^+/(k_F \Pi^+) \approx 1$ for $\mathrm{Ro} > 1$ (both quantities direct cascade), while as the Rossby number decreases $\Sigma^+/k_F > \Pi^+$.

We can also introduce the differences between the direct and inverse energy and helicity fluxes, respectively, as $\Delta\Sigma = (\Sigma^+ - \Sigma^-)/k_F$ and $\Delta\Pi = \Pi^+ - \Pi^-$ (where Σ^- and Π^- are negative and denote, respectively, the amount of helicity and energy that go towards large scales). Figure 6 shows the normalized ratio

$$\rho = (\Delta\Sigma + \Delta\Pi)/\Delta\Sigma.$$

This ratio is roughly independent of the Rossby number, which further confirms that the dominance of the helicity flux for $k > k_F$ is associated with the energy flux lost in that range because of the inverse cascade of energy.

As a result, the direct transfer in the small scales of a rotating helical turbulent flow is dominated by the (normalized) helicity flux. In the limit of a pure helicity cascade with no direct energy cascade, and considering the effect of rotation, the helicity flux can be expressed as

$$\Sigma(k) \sim \delta \sim \frac{h_l}{\tau_l^2} \tau_\Omega, \tag{16}$$

where h_l is the helicity at the scale l, $\tau_l \sim l/u_l$ is the eddy turnover time at the same scale, and $\tau_\Omega \sim 1/\Omega$ is the characteristic time of inertial waves. This expression takes into account the slowing-down of transfer to small scales due to three-wave interactions (see, e.g., Refs. [32,33]), in a similar fashion as what was proposed by Iroshnikov and Kraichnan for Alfvén waves in the presence of a magnetic field [34,35] (the extension to the anisotropic case can be trivially obtained considering the turnover time as $\tau_l \sim l_\perp/u_l$, see, e.g., Ref. [33]). From this expression, it follows that if $E(k) \sim k^{-n}$ ($n \leqslant 2.5$, with the equality holding for the case with maximum helicity at all scales from Schwarz inequality), then

$$H(k) \sim k^{n-4}, \tag{17}$$

i.e., resulting in a shallower helicity spectrum for $n \geqslant 2$ (note that for $n < 2$ the helicity spectrum is steeper than the energy spectrum).

Although the runs in set A have a helicity spectrum that is indeed slightly shallower than the energy spectrum, the forcing is applied at intermediate scales and the scale separation between the forcing and dissipative scales is not enough to confirm the scaling prediction of Eq. (17). Indeed, the micro-

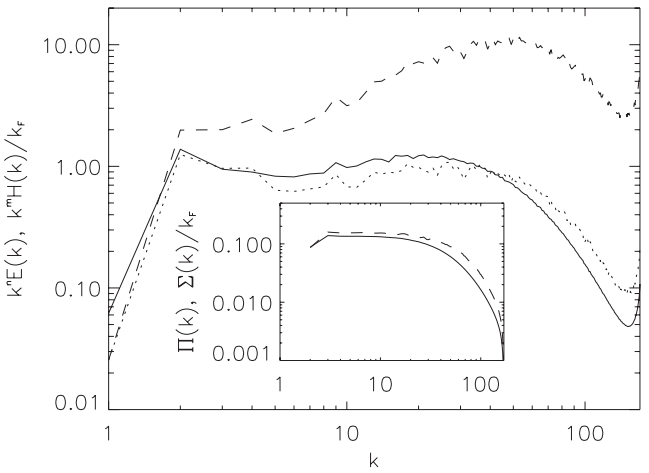

FIG. 7. Energy spectrum compensated by k^n with $n=5/3$ (solid), helicity spectrum compensated by k^m with $m=n$ (dots), and compensated by $m=n-4\approx 2.33$ (dash line), in run B1 with large-scale forcing and weak rotation. Note that the helicity and the energy in this run have the same Kolmogorov scaling in the inertial range. The inset shows the energy and normalized helicity fluxes with solid and dash lines, respectively.

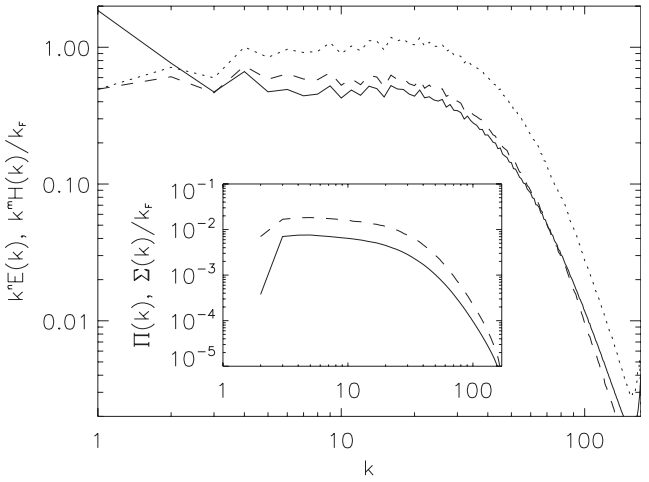

FIG. 8. Energy spectrum compensated by k^n with $n=2.15$ (solid), helicity spectrum compensated by k^m with $m=n$ (dot), and compensated by $m=n-4=1.85$ (dash line), in run B2 with large-scale forcing and low Rossby number. Note that the helicity and the energy spectra in this run have different scalings in the inertial range (different from each other and different from K41), and both are flat only when compensated following Eq. (17). The inset again shows the energy and (normalized) helicity fluxes; note the domination of the latter in this high-rotation regime.

Rossby numbers are $\mathrm{Ro}_\omega\approx 0.6$ for run A3 and ≈ 0.2 for run A4 (see Table II). A larger direct inertial range and larger micro-Rossby numbers are needed in order to check the validity of the predicted scaling.

To that effect, we now report on the runs in set B (see Tables I and II) which have a forcing function concentrated in the large scales; the inverse cascade is thus not so well resolved but it allows for a more developed direct inertial range. In particular, we will focus on run B2 which has a Rossby number $\mathrm{Ro}\approx 0.05$ and a micro-Rossby number $\mathrm{Ro}_\omega \approx 1.1$. Figures 7 and 8 show the compensated energy and helicity spectra for runs B1 and B2 (run B3 behaves as run A3). It is observed that while in run B1 (corresponding to weak rotation), the helicity and energy spectra have the same scaling ($\sim k^{-5/3}$ with bottleneck and intermittency corrections), in run B2 the compensated helicity and energy spectra are horizontal and parallel only when using the scaling law predicted by Eq. (17).

The same scaling is observed in $k_\perp$. As previously mentioned, it is straightforward to recast Eqs. (16) and (17) to take into account the anisotropies in the flow, again similarly to the magnetohydrodynamic case. The results exemplified by Fig. 8 confirm that the small-scale scaling of energy and helicity differ in rotating turbulence, unlike the nonrotating case (see, e.g., Fig. 7) where energy and helicity follow the same spectral laws.

IV. CONCLUSION

Even though the Rossby number in the atmosphere of the Earth is not very large, the existence of inertial waves that can interact with turbulent eddies is bound to affect the dynamics of the turbulent flow, as has been studied by several authors. Helicity, which is also observed in atmospheric flows, is known to play an important role in the evolution of tornadoes. But, as already found in Ref. [19], the two physical phenomena (rotation on the one hand, helicity on the other hand) reduce nonlinear interactions in different ways. Thus a study combining both effects at high Reynolds number can shed some light on the dynamics of such flows.

This paper shows that for strong rotation, the direct cascade to small scales is now dominated by the helicity flux (and the inverse cascade, as expected, by the energy). Moreover, the resulting spectrum is different from what Kolmogorov scaling predicts for the nonrotating case, and from what a pure direct cascade of energy slowed down by eddy-wave interactions predicts for the rotating nonhelical case. In this context it is worth mentioning that, using phenomenological arguments, a direct cascade of helicity in rotating flows has also been argued recently in Ref. [36], although the arguments predicted a different scaling and were based on Fjortoft's theorem [37,38] which does not necessarily apply to the helicity since it is not a positive definite quantity [5].

A phenomenological argument based on a cascade of helicity towards small scales slowed down by wave-eddy interactions lead to different inertial indices for the small-scale energy and helicity spectra, and provides a good fit to the results of the simulations presented in this paper. The spectral indices are bounded by the value that corresponds to a flow with maximum helicity, and depend on the amount of relative helicity in the flow. The result differs from nonrotating turbulence, where the energy and the helicity follow the same scaling laws [4,8,10]. Although the DNS runs confirm the scaling, due to computational limitations well-resolved inverse and direct cascades had to be studied in separate simulations. In the future, a simulation of helical rotating turbulence at very large resolution will be performed to confirm these results with a better resolved coexistence of the direct and inverse cascades.

At this point, it may be of interest to compare our results with previous studies of rotating helical turbulence. Reference [18] studied rotating turbulence in the limit of small Rossby number using weak turbulence theory. For the anisotropic case, spectra $E \sim k_\perp^{-5/2} k_\parallel^{-1/2}$ and $H \sim k_\perp^{-3/2} k_\parallel^{-1/2}$ result. As in our simulations, and unlike nonrotating turbulence, the spectrum of helicity in this theory is found to be different from the energy spectrum. Considering that most of the energy in our simulations is in $k_\perp$ modes, the scaling in $k_\perp$ is consistent with our results for the case of maximum helicity ($n=2.5$). However, care must be taken since our simulations were done for moderate values of the Rossby number. Also, the scaling laws obtained in Ref. [18] are independent of the helicity content of the flow, while our simulations seem to indicate a different behavior for helical and nonhelical rotating flows. These differences may be the result of the moderate values of the Rossby number studied here, or of the lack of an inverse cascade of energy (which plays an important role in our phenomenological arguments) at the lowest order in the expansion considered in Ref. [18]. Further studies will be needed to answer these questions.

Morinishi *et al.* [19] also considered helical rotating flows, although in freely decaying simulations. The authors observed a difference in the decay of helical and nonhelical rotating turbulence, and interpreted this as the result of distinct mechanisms in each case: the decrease in the energy transfer by phase mixing associated to the rotation, and the global quenching of the direct energy flux by the alignment of velocity and vorticity associated to the helicity. These results are also in qualitative agreement with the phenomenological theory discussed here, although the simulations in Ref. [19] were stopped shortly after the peak of dissipation and the self-similar decay of the flows was not studied. A study of the different phases of freely decaying helical rotating flows in the light of this results is currently under way.

The study of the intermittency of a mixture of turbulence and waves in the presence of rotation and helicity will also be the topic of a future work; it is of particular interest since it will shed some light on the statistics, structures, and interactions of extreme events which, when combined with realistic physics of the atmosphere (e.g., adding weak compressibility, moisture, and geometry), will lead eventually to a better understanding and prediction of the behavior of atmospheric flows.

ACKNOWLEDGMENTS

Computer time was provided by NCAR. NCAR is sponsored by the National Science Foundation. P.D.M. acknowledges support from Grant No. UBACYT X468/08 and from the Carrera del Investigador Cientifico of CONICET.

[1] A. N. Kolmogorov, Dokl. Akad. Nauk SSSR **30**, 9 (1941).
[2] H. K. Moffatt, J. Fluid Mech. **35**, 117 (1969).
[3] R. Betchov, Phys. Fluids **4**, 925 (1961).
[4] A. Brissaud, U. Frisch, J. Léorat, M. Lesieur, and A. Mazure, Phys. Fluids **16**, 1366 (1973).
[5] R. H. Kraichnan, J. Fluid Mech. **59**, 745 (1973).
[6] J. C. André and M. Lesieur, J. Fluid Mech. **81**, 187 (1977).
[7] V. Borue and S. A. Orszag, Phys. Rev. E **55**, 7005 (1997).
[8] Q. Chen, S. Chen, and G. L. Eyink, Phys. Fluids **15**, 361 (2003).
[9] Q. Chen, S. Chen, G. L. Eyink, and D. D. Holm, Phys. Rev. Lett. **90**, 214503 (2003).
[10] D. O. Gómez and P. D. Mininni, Physica A **342**, 69 (2004).
[11] P. D. Mininni, A. Alexakis, and A. Pouquet, Phys. Rev. E **74**, 016303 (2006).
[12] C. Cambon and L. Jacquin, J. Fluid Mech. **202**, 295 (1989).
[13] F. Waleffe, Phys. Fluids A **5**, 677 (1993).
[14] A. Craya, *Contribution à l'analyse de la Turbulence Associée à des Vitesses Moyennes* (P.S.T. Ministère de l'Air, Paris, France, 1958), Vol. 345.
[15] J. Herring, Phys. Fluids **17**, 859 (1974).
[16] C. Cambon, N. N. Mansour, and F. S. Godeferd, J. Fluid Mech. **337**, 303 (1997).
[17] L. M. Smith and F. Waleffe, Phys. Fluids **11**, 1608 (1999).
[18] S. Galtier, Phys. Rev. E **68**, 015301(R) (2003).
[19] Y. Morinishi, K. Nakabayashi, and S. Ren, JSME Int. J., Ser. B **44**, 410 (2001).
[20] D. K. Lilly, J. Atmos. Sci. **43**, 126 (1988).
[21] B. W. Kerr and G. L. Darkow, Weather Forecast. **11**, 489 (1996).
[22] P. M. Markowski, J. M. Straka, E. N. Rasmussen, and D. O. Blanchard, Mon. Weather Rev. **126**, 2959 (1998).
[23] P. D. Mininni, A. Alexakis, and A. Pouquet, Phys. Fluids **21**, 015108 (2009).
[24] D. O. Gómez, P. D. Mininni, and P. Dmitruk, Adv. Space Res. **35**, 899 (2005).
[25] D. O. Gómez, P. D. Mininni, and P. Dmitruk, Phys. Scr. **T116**, 123 (2005).
[26] S. Childress and A. D. Gilbert, *Stretch, Twist, Fold: The Fast Dynamo* (Springer-Verlag, Berlin, 1995).
[27] V. Archontis, S. B. F. Dorch, and A. Nordlund, Astron. Astrophys. **410**, 759 (2003).
[28] H. K. Moffatt, *Magnetic Field Generation in Electrically Conducting Fluids* (Cambridge University Press, Cambridge, 1978).
[29] F. S. Godeferd and L. Lollini, J. Fluid Mech. **393**, 257 (1999).
[30] L. Jacquin, O. Leuchter, C. Cambon, and J. Mathieu, J. Fluid Mech. **220**, 1 (1990).
[31] H. P. Greenspan, J. Fluid Mech. **36**, 257 (1969).
[32] Y. Zhou, Phys. Fluids **7**, 2092 (1995).
[33] W.-C. Müller and M. Thiele, Europhys. Lett. **77**, 34003 (2007).
[34] P. S. Iroshnikov, Sov. Astron. **7**, 566 (1963).
[35] R. H. Kraichnan, Phys. Fluids **8**, 1385 (1965).
[36] S. Chakraborty, Europhys. Lett. **79**, 14002 (2007).
[37] R. Fjortoft, Tellus **5**, 225 (1953).
[38] M. Lesieur, *Turbulence in Fluids* (Kluwer Academic Press, Dordrecht, 1997).